

1 Article

2 **Si-disordering in MgAl₂O₄-spinel at high *P-T*
3 conditions, with implication to Si-Mg disorder in
4 Mg₂SiO₄-ringwoodite**

5 **Liping Liu^{1,2}, Xi Liu^{1,2*}, Xinjian Bao^{1,2}, Qiang He³, Wei Yan^{1,2,4}, Yunlu Ma^{1,2},
6 Mingyue He⁴, Renbiao Tao⁵ and Ruqiang Zou⁶**

7 ¹School of Earth and Space Sciences, Peking University, Beijing 100871, China

8 ²Key Laboratory of Orogenic Belts and Crustal Evolution, Ministry of Education of China,
9 Beijing 100871, China

10 ³Institute of Fluid Physics, China Academy of Engineering Physics, Mianyang 659000,
11 China

12 ⁴School of Gemmology, China University of Geosciences (Beijing), Beijing 100083, China

13 ⁵Geophysical Laboratory, Carnegie Institution of Washington, Washington, D.C. 20015,
14 U.S.A.

15 ⁶Beijing Key Lab of Theory and Technology for Advanced Battery Materials, Department
16 of Material Science and Engineering, College of Engineering, Peking University, Beijing
17 100871, China

18

19 *Corresponding Author: Xi Liu

20 Email: xi.liu@pku.edu.cn Tel: 86-10-6275-3585 Fax: 86-10-6275-2996

21 **Abstract:** A series of Si-bearing MgAl₂O₄-spinels were synthesized at 1500-1650 °C
22 and 3-6 GPa. These spinels had SiO₂ contents up to ~1.03 wt%, and showed a
23 substitution mechanism of Si⁴⁺ + Mg²⁺ = 2Al³⁺. Unpolarized Raman spectra were
24 collected from polished single grains, and displayed a set of well-defined Raman
25 peaks at ~610, 823, 856 and 968 cm⁻¹ which had not been observed before. Aided
26 with the Raman features of natural Si-free MgAl₂O₄-spinel, synthetic Si-free
27 MgAl₂O₄-spinel, natural low quartz, synthetic coesite, synthetic stishovite and
28 synthetic forsterite, we infer that these Raman peaks should belong to the SiO₄
29 groups. The relations between the Raman intensities and SiO₂ contents of the
30 Si-bearing MgAl₂O₄-spinels suggest that at some *P-T* conditions some Si must adopt
31 the M-site. Unlike the SiO₄ groups with very intense Raman signals, the SiO₆ groups
32 are largely Raman-inactive. We have further found that the Si cations primarily
33 appear on the T-site at *P-T* conditions \leq ~3-4 GPa and 1500 °C, but attain a random
34 distribution between the T-site and M-site at *P-T* conditions \geq ~5-6 GPa and
35 1630-1650 °C. This Si-disordering process observed for the Si-bearing
36 MgAl₂O₄-spinels hints that similar Si-disordering might happen to the
37 (Mg,Fe)₂SiO₄-spinels (ringwoodite), the major phase in the lower part of the mantle
38 transition zone of the Earth and the index mineral for the very strong shock stage
39 experienced by extraterrestrial materials. The likely consequences have been
40 explored.

41 **Keywords:** 4-coordinated Si; 6-coordinated Si; MgAl₂O₄-spinel; Mg₂SiO₄-ringwoodite;
42 Raman spectroscopy; Si-disordering
43

44 **1. Introduction**

45 Spinel (Sp; AB₂O₄) *sensu lato* plays a crucial role in Earth sciences. The so-called
46 2-3 Sp, A = 2+ cations and B = 3+ cations, is ubiquitous in most terrestrial rocks [1,2].
47 With significant compositional complexity and wide *P-T* stability field, it
48 participates many phase equilibria, which can be calibrated as geothermometers,
49 geobarometers and oxybarometers [3-5], and therefore has many geological
50 implications. Taking the chromian Sp as an example, it has been widely used as a
51 "petrological litmus paper" to classify upper mantle peridotites, explore melt
52 compositional characteristics of the upper mantle, probe crystallization processes of
53 basaltic magmas, and estimate *P-T* conditions of diamond formation [6-9].
54 Additionally, the 2-3 Sp is widely observed on some extraterrestrial planets,
55 asteroids and meteorites [10-14]. Furthermore, it is even found as one of the major
56 phases in some lunar rocks or lunar meteorites [15,16], implying some special
57 features of the magma's evolution history of the Moon.

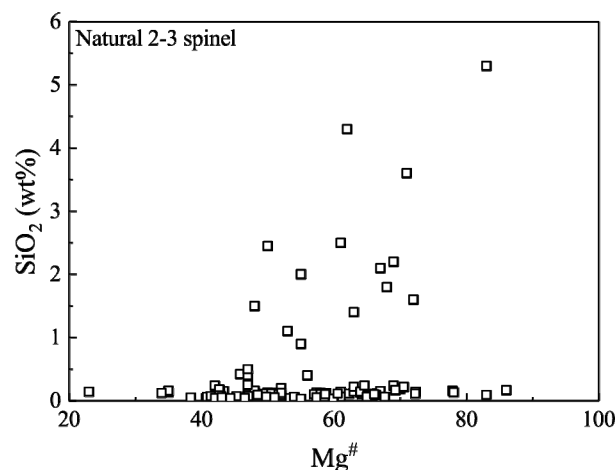
58 Less frequently observed, the so-called 4-2 Sp (A = 4+ cations and B = 2+ cations)
59 is also geologically important, with the (Mg,Fe)₂SiO₄-Sp (or ringwoodite; Rw) being
60 the most distinct example. It has been accepted that Rw with an Mg[#] of ~89 (Mg[#] =
61 100Mg/(Mg+Fe); molar ratio) is the most abundant phase in the lower part of the
62 mantle transition zone (LP-MTZ; ~520-660 km). The physical-chemical properties of
63 the Rw thus have significant implications in building the mineralogical models of
64 the Earth's deep interior, constraining the origins of the 520-km and 660-km seismic
65 discontinuities, and exploring the rheological behavior and convection process of
66 the MTZ [17-21]. Recent discovery of a terrestrial Rw crystal included in a diamond
67 confirms the superior role that Rw plays [22]. In comparison, extraterrestrial Rw has
68 been commonly documented in L ordinary chondrites ([23]; and references therein),
69 and less frequently recorded in H ordinary chondrites [24,25], LL ordinary
70 chondrites [14,26], CV carbonaceous chondrite [27], and CB carbonaceous chondrite
71 [28]. Furthermore, it has been observed in some lunar meteorites [29,30] and many
72 Martian meteorites (for Rw in the shergottite, see Boonsue & Spray [31], Baziotis et
73 al. [32], Greshake et al. [33], Walton [34], Walton et al. [35], Ma et al. [36,37], and
74 Miyahara et al. [38]; for Rw in the chassigny, see Fritz & Greshake [12]). Rw has
75 been proposed as the index mineral for the very strong shock stage experienced by
76 the meteorites (S6; [39]), and its discoveries have set important constraints on the
77 shock *P-T* conditions, shock durations, and sizes of the impactors, which may be
78 combined with the radiometric ages of the shock events to provide valuable
79 knowledge for the theoretical evolution models of the early solar system [23,40,41].
80

81 One distinct feature of the structure of Sp is its order-disorder phenomenon. Sp
82 has the space group $Fd\bar{3}m$, and has two symmetrically different metal sites
83 (tetrahedral and octahedral sites, with 1/8 of the former and 1/2 of the latter
84 occupied by cations; T-site and M-site hereafter), so that its structural formula is
85 usually written as $^{[4]}A^{[6]}B_2O_4$. The cations on these two sites readily switch positions,
86 and Sp becomes disordered, leading to a more general formula $^{[4]}(A_{1-x}B_x)^{[6]}(A_xB_{2-x})O_4$,
87 where x is the inversion parameter ($x = 0 \rightarrow$ normal Sp; $x = 1 \rightarrow$ inverse Sp; $x = 0.667 \rightarrow$
88 completely-disordered Sp). This order-disorder process is complicated, and
89 influences many elastic, thermodynamic and thermochemical properties [19,42-46].

90 The order-disorder status of the 2-3 $MgAl_2O_4$ -Sp, the archetype of all spinels,
91 can be significantly affected by T , P , composition, and even grain size. The
92 $MgAl_2O_4$ -Sp is generally a normal Sp at ambient condition, but becomes partially or
93 even fully disordered as T and P increase [42,43,45,47-57]. Its inversion parameter x
94 increases as its grain size decreases [58]. Additionally, there have been some
95 preliminary discussions on the effect of composition [42,53]. In contrast, the
96 order-disorder issue of the 4-2 Mg_2SiO_4 -Sp (Rw) is still hotly debated, and
97 convincing evidence to the presence of 6-coordinated Si remains at large. From
98 knowledge on ionic radius systematics and thermodynamic considerations
99 [19,59,60], a small amount of structural disorder was suggested, with x reaching
100 ~0.02-0.04 for the $P-T$ conditions of the LP-MTZ. However, high-resolution ^{29}Si MAS
101 NMR data indicated no 6-coordinated Si [61], a result potentially affected by a fast
102 structural reequilibrating during sample-quenching process. Nevertheless, the Rw
103 grains in the highly-shocked L6-type ordinary chondrites NWA 1662 and NWA 463,
104 with distinct and different colors, showed clues of structural inversion [62], which
105 was partially preserved presumably due to much larger cooling rates. Considering
106 the large influence of the x parameter on the elastic constants, elastic anisotropy,
107 and seismic velocities [19,46,63], the Mg-Si order-disorder process deserves more
108 investigation, which is the focus of this study.

109 In Sp, the size of a cation has a profound influence in determining its site
110 preference, with larger ions to prefer the T-site of the 2-3 Sp, but to prefer the M-site
111 of the 4-2 Sp [59]. With a relatively small size difference between the Mg and Al
112 cations in the $MgAl_2O_4$ -Sp, the cation disorder achieved at high $P-T$ conditions can
113 be partially preserved [42,45,48,50,51,53]. In contrast, the relatively large size
114 difference between the Mg and Si cations in the Rw may strengthen this
115 size-dependent site preference, and accelerate the cation-redistribution process
116 during cooling, so that the cation disorder attained at high $P-T$ conditions may be
117 easily lost, leading to null signals for cation disorder, as experimentally observed
118 [61,64]. To circumvent this obstacle, we have taken an indirect approach by doping
119 the $MgAl_2O_4$ -Sp with some Si, and examined if Si can be disordered. It has been
120 expected that silicon can readily enter the $MgAl_2O_4$ -Sp, for the SiO_2 in natural 2-3 Sp
121 reaches up to ~5.3 wt% (Fig. 1). In this study, we first synthetized the Si-bearing
122 $MgAl_2O_4$ -Sp at high P . We then analyzed the experimental products by Raman
123 spectroscopy, a powerful method to study cation-disordering [49,57]. To facilitate

124 data interpretation, natural Si-free MgAl_2O_4 -Sp (N-Sp), natural low quartz (N-Qz),
 125 and synthetic Si-free MgAl_2O_4 -Sp, coesite (Coe), stishovite (St) and forsterite (Fo)
 126 were similarly analyzed. Here we report the first experimental evidence for the
 127 6-coordinated Si in the Sp structure.



128
 129 **Figure 1.** SiO_2 (wt%) vs $\text{Mg}^{\#}$ of some natural 2-3 spinels. $\text{Mg}^{\#}$, $100\text{Mg}/(\text{Mg}+\text{Fe})$ in
 130 molar ratio. Data sources are Sigurdsson et al. [65], Sobolev & Nikogosian [66],
 131 Kamenetsky et al. [67], Franz & Wirth [68], and Chistyakova et al. [69].

132 2. Experimental and analytical methods

133 High- P experiments were conducted on a cubic press at the High-Pressure
 134 Laboratory of Peking University [70] and a multi-anvil press at the Geophysical
 135 Laboratory, Carnegie Institution of Washington [71]. With the experimental
 136 charges encapsulated in sealed Pt tubes, a series of Si-bearing MgAl_2O_4 -Sp were
 137 synthesized in the system $\text{CaO}-\text{MgO}-\text{Al}_2\text{O}_3-\text{SiO}_2-\text{K}_2\text{O}-\text{CO}_2$ at 3-6 GPa and 1500-1650
 138 °C by employing conventional electrical resistance heating technique (Table 1). In
 139 addition, we used the high- P experimental techniques to separately synthesize
 140 Si-free MgAl_2O_4 -Sp, Coe and St (Table 1). The P and T uncertainties in our high- P
 141 experiments should be better than ~0.5 GPa and 50 °C [70-72].

142 **Table 1.** Experimental conditions, phase assemblages, and compositions of spinels and quartz (wt%)

143	Exp. #	P^a	T^a	t^a	Phase assemblage	MgO	Al_2O_3	SiO_2	Total
144	LMD565	3	1500	36	Sp(8) ^b +Melt	28.66(25) ^c	70.23(53)	0.39(5)	99.29(72)
145	LMD564	4	1500	36	Sp(8)+Melt	29.26(15)	70.29(18)	0.65(7)	100.22(33)
146	LMD563	4	1550	24	Sp(7)+Melt	28.44(22)	70.92(33)	0.30(7)	99.68(35)
147	LMD558	4	1550	36	Sp(5)+Fo+Melt	29.01(30)	69.98(60)	0.76(3)	99.75(86)
148	LMD578	5	1630	12	Sp(13)+Grt+Melt	28.94(18)	70.22(25)	0.76(7)	99.92(36)
149	LMD568	6	1650	12	Sp(13)+Grt+Melt	29.13(26)	69.27(59)	1.03(7)	99.45(78)
150	LMD487 ^d	5	1600	12	Sp	--	--	--	--

151	LMD659 ^e	5	1500	12	Coe+Melt	--	--	--	--
152	PL1316 ^e	14	1400	8	St	--	--	--	--
153									
154	Natural spinel			N-Sp(10)		28.05(18)	70.81(22)	0.01(1)	100.03(39)
155	Natural quartz			N-Qz(10)		0.00(1)	0.13(9)	100.95(51)	101.17(57)

^a*P*, pressure in GPa; *T*, temperature in °C; *t*, time in hour.

^bNumber in the parenthesis after the name of the phase is the number of successful EMP analyses performed on that phase. Sp, spinel; Melt, silicate melt; Fo, forsterite; Grt, garnet; Coe, coesite; St, stishovite; Qz, quartz.

^cNumber in the parenthesis is the analytical uncertainty reported as one standard deviation. 28.66(25) read as 28.66 ± 0.25.

^dStarting material is a mixture of dried high purity MgO and Al₂O₃ powders, weighted out according to the stoichiometry of the MgAl₂O₄ spinel.

^eStarting material is a dried high purity SiO₂ powder, with some water added later.

The compositions of the crystalline phases from the high-*P* experiments were obtained by using a JXA-8100 electron microprobe (EMP) in wavelength dispersive mode (WDS). For all the EMP analyses, the beam current was 10 nA, the accelerating voltage 15 kV, the beam spot size 1 μm, and the counting time 40 s. Calibration was based on optimization to some standards provided by the SPI Corporation (USA), with diopside for Mg and Ca calibrations, jadeite for Si, Al and Na calibrations, chromium oxide for Cr calibration, hematite for Fe, sanidine for K, rutile for Ti, rhodonite for Mn, and nickel silicide for Ni. Data correction was performed with the PRZ method. The results are shown in Table 1 (the CaO and K₂O contents below the detection limits).

Two natural gem-quality mineral samples were employed in this study as well: one was a red, Si-free Sp crystal (N-Sp) with an octahedral shape from Mogok (Burma), and the other was a clear low Qz crystal (N-Qz) from Donghai (China). Both were similarly analyzed for compositions with the EMP in the WDS mode. Besides the components shown in Table 1, extra components in the N-Sp included 0.06(3)% TiO₂, 0.95(6)% Cr₂O₃ and 0.10(1)% FeO, leading to the chemical formula (Mg_{0.993}Fe_{0.002}Ti_{0.001})(Al_{1.983}Cr_{0.018})O₄ (all iron assumed as Fe²⁺). Extra components in the N-Qz were below the detection limits.

Unpolarized Raman spectra were collected from 100 to 1350 cm⁻¹ with a Renishaw inVia Reflex system in a back-scattering geometry at ambient *P-T* conditions. A 532 nm laser with an emission power of ~50 mW and a 50× long-distance objective were used in all analyses. Other analytical conditions were ~1 μm light spot, 1 cm⁻¹ spectral resolution, and 20 successive scans for every analysis (10 s for each scan). For every high-*P* product, multiple analyses were conducted on well-polished and arbitrarily-selected Sp, Coe, St and Fo grains with unknown orientations. In comparison, the Raman spectrum of the N-Sp was

192 collected from the (111) plane whereas that of the N-Qz was from the (001) plane.
193 The Raman data were processed by using the PeakFit V4.12 software (SPSS Inc.).

194 In addition, we analyzed one fragment of the N-Sp for its order-disorder state
195 by single-crystal XRD method. Data were collected using an Agilent Technologies
196 Rigaku micro-focused diffractometer (Mo K α radiation; $\lambda = 0.71073$ nm), and
197 processed using the SHELXT software included in the SHELXTL package. From the
198 single-crystal XRD data we directly obtained an x value of 0.129, probably with
199 relatively large uncertainty due to the similar scattering factors of Mg and Al.
200 Following the method of Carbonin et al. [73], with the bond distances from Lavina
201 et al. [74] and with $x = 0.129$ as one of the input variables, further, we calculated a
202 new x value, which was in turn used as an input in the next round of crystal
203 structural analysis. The final cycles of the least-squares refinement, including
204 atomic coordinates and anisotropic thermal parameters for the atoms [$I > 2\text{sigma}(I)$],
205 converged at $R_1 = 0.0164$, $wR_2 = 0.0730$ and $S = 1.065$, and yielded $x = 0.162$ (see
206 Supplementary Material for the details). Using the empirical equation proposed by
207 Andreozzi & Princivalle [55],

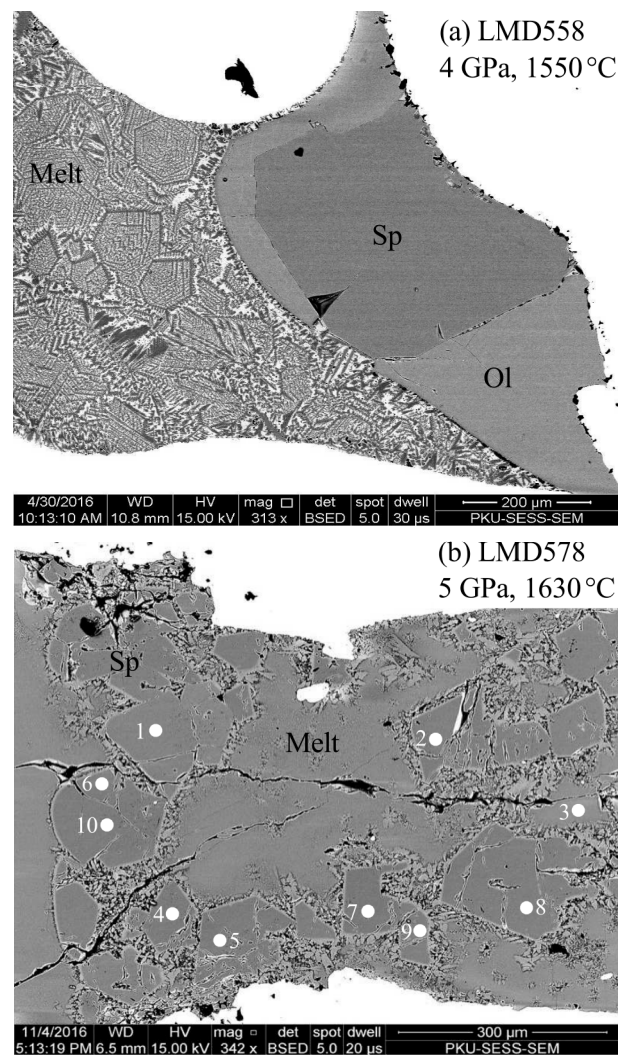
208
$$x = 21.396 - 80.714u \quad (1),$$

209 where u is the oxygen positional parameter in the Sp structure ($u = 0.26329(24)$ for
210 our N-Sp), alternatively, we constrained the x value as 0.145. $x = 0.145$ is preferred
211 in this study.

212 3. Results and discussions

213 3.1 Synthetic MgAl₂O₄-Sp and its SiO₂

214 In total, nine high- P experiments with long durations were conducted (Table 1):
215 six of them for synthesizing Si-bearing MgAl₂O₄-Sp, one for Si-free MgAl₂O₄-Sp,
216 one for Coe, and one for St. In the synthesizing experiments for the Si-bearing
217 MgAl₂O₄-Sp, a CO₂-rich melt phase with intense quench-modification texture was
218 always observed. Some other crystalline phases like Fo and garnet (Grt) were
219 occasionally detected. The crystalline phases in all these experiments had large
220 grain sizes up to ~600 μm , showed sharp grain boundaries and attained
221 homogeneous chemical compositions. Typical electron back-scatter images from
222 some of these experiments are shown in Fig. 2. In the experiments for the Si-free
223 MgAl₂O₄-Sp, Coe and St, a melt phase was clearly observed in LMD659 only (Table
224 1). The grain boundaries of the Si-free MgAl₂O₄-Sp, Coe and St were well defined,
225 their grain sizes large (up to ~100 μm in diameter), and their compositions expected
226 to be homogeneous.



227

228 **Figure 2.** Typical electron back-scatter images: (a) LMD558 at 4 GPa and 1550 °C; (b)
 229 LMD578 at 5 GPa and 1630 °C. On the exposed sample surface of LMD558, we
 230 observed just one large Sp grain, surrounded by olivine compositionally
 231 approximating Fo ($Mg_{2.034(30)}Ca_{0.004(0)}Si_{0.973(15)}Al_{0.011(1)}O_4$; five EMP analyses). In contrast,
 232 many Sp grains were found on the exposed sample surface of LMD578, coexisting
 233 with Grt grains (not shown in (b); $Mg_{2.765(66)}Ca_{0.294(67)}Al_{1.968(18)}Si_{2.995(11)}O_{12}$, based on 10
 234 EMP analyses). The white spots numbered from 1 to 10 in (b) represent the
 235 positions, where the Raman spectra shown in Fig. 7b were taken.

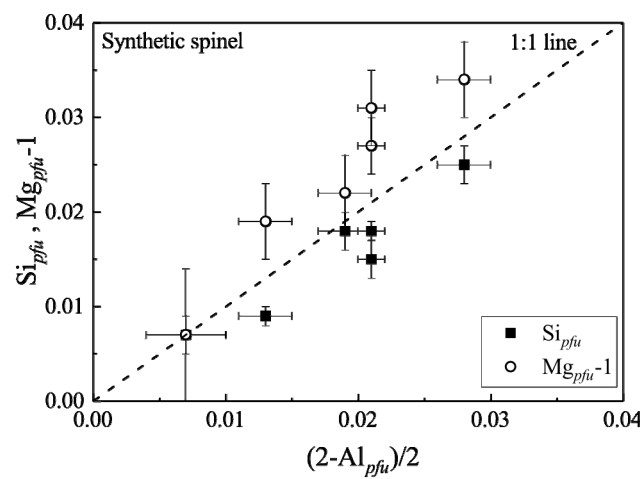
236

237 With up to ~1 wt% SiO_2 (Table 1), the compositions of the Si-bearing
 238 $MgAl_2O_4$ -Sp are shown in Fig. 3. A primary observation here is that one Si^{4+} and one
 239 Mg^{2+} substitute for two Al^{3+} ,



241 In detail, the (Si_{pfu}) values seem slightly lower than the (Mg_{pfu} -1) values, which
 242 perhaps relates to the compositional characteristics of the coexisting phase(s).
 243 Nevertheless, the effects of P , T and coexisting phases on this cation substitution
 244 reaction are not clear, but presently under a thorough experimental investigation.

245 The cation radii of Mg (r_{Mg}), Al (r_{Al}) and Si (r_{Si}) are very different, $r_{\text{Mg}} = 0.585 \text{ \AA} > r_{\text{Al}} =$
 246 $0.39 \text{ \AA} > r_{\text{Si}} = 0.275 \text{ \AA}$ on the T-site and $r_{\text{Mg}} = 0.715 \text{ \AA} > r_{\text{Al}} = 0.53 \text{ \AA} > r_{\text{Si}} = 0.40 \text{ \AA}$ on the
 247 M-site at ambient conditions [59]. Since larger ions prefer the T-site of the 2-3 Sp, the
 248 Si-free MgAl_2O_4 -Sp should generally adopt a normal Sp structure, as verified by
 249 some studies on natural Sp with compositions close to the MgAl_2O_4 formula ($x =$
 250 $\sim 0.02\text{--}0.04$ in Schmocker & Waldner [47]; $x = 0.05$ in Maekawa et al. [51]). By the
 251 same token, Si in the MgAl_2O_4 -Sp should occupy the M-site. However, existing
 252 single-crystal XRD studies on natural 2-3 Sp locate Si on the T-site [73,75-77]. The
 253 coupled substitution of Si and Mg for 2Al as observed in our high- P synthetic
 254 MgAl_2O_4 -Sp and the site-occupation knowledge to be revealed by our Raman
 255 spectroscopic data should shed light on the Si distribution.



256

257 **Figure 3.** Si_{pfu} and $\text{Mg}_{\text{pfu-1}}$ vs $(2\text{-Al}_{\text{pfu}})/2$ of synthetic spinels from our high- P
 258 experiments. pfu stands for per formula unit.

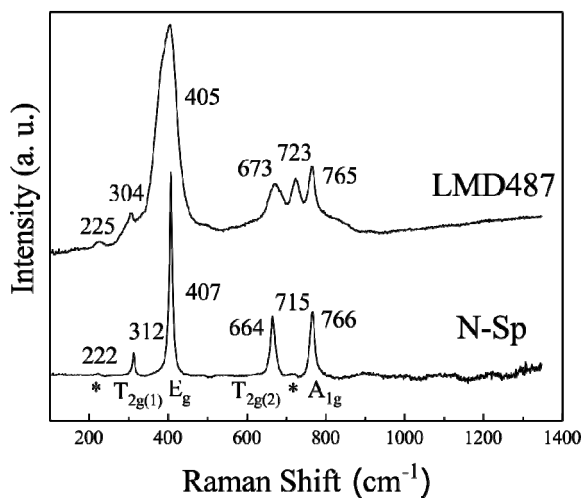
259

260 3.2 Raman features of nearly normal MgAl_2O_4 -Sp

261 There are two chemical formula units per primitive unit cell of normal
 262 MgAl_2O_4 -Sp (14 atoms), which leads to three acoustic modes and 39 optic modes
 263 according to group theory. Five Raman-active fundamental vibrations, $\text{A}_{1g} + \text{E}_g +$
 264 3T_{2g} , are predicted [78]. Theoretical calculations yield the A_{1g} at $\sim 762 \text{ cm}^{-1}$, E_g at ~ 408
 265 cm^{-1} , and T_{2g} at $\sim 667 \text{ cm}^{-1}$ ($\text{T}_{2g(2)}$), $\sim 557 \text{ cm}^{-1}$ ($\text{T}_{2g(3)}$) and $\sim 317 \text{ cm}^{-1}$ ($\text{T}_{2g(1)}$; [79-85]). The
 266 intensity of these Raman modes decreases in the order of $\text{E}_g > \text{T}_{2g(2)} > \text{A}_{1g} > \text{T}_{2g(1)} > \text{T}_{2g(3)}$
 267 [83]. Except the weakest $\text{T}_{2g(3)}$ peak, all other four peaks were routinely observed on
 268 natural MgAl_2O_4 -Sp with very low and insignificant amounts of impurities like SiO_2 ,
 269 TiO_2 , Cr_2O_3 , FeO and/or ZnO [49,57,78,86,87].

270 Our N-Sp displays four sharp peaks at ~ 312 , 407 , 664 and 766 cm^{-1} , compatible
 271 with the Raman features established for normal MgAl_2O_4 -Sp (Fig. 4). Furthermore,
 272 two weak and broad peaks are observed at ~ 222 and 715 cm^{-1} , which are attributable
 273 to the slightly-disordered structural feature ($x = 0.145$). The small peak at $\sim 715 \text{ cm}^{-1}$
 274 was also evident in the Raman spectra of the natural MgAl_2O_4 -Sp studied by
 275 Chopelas & Hofmeister [78] and by Cynn et al. [86]. Both samples attained some

276 structural disorder: using Equation (1), the x value of the former sample is
 277 calculated as ~ 0.144 ($u = 0.2633$); the x value of the latter sample was claimed as
 278 ~ 0.02 , which might have been slightly underestimated (more discussion later). On
 279 the other hand, it was not observed for the natural $\text{MgAl}_2\text{O}_4\text{-Sp}$ studied by Cynn et
 280 al. [49], Van Minh & Yang [87] or Slotznick & Shim [57], implying x values at least
 281 smaller than ~ 0.145 . No Raman spectra previously collected on unannealed natural
 282 $\text{MgAl}_2\text{O}_4\text{-Sp}$ showed the weak peak at $\sim 222 \text{ cm}^{-1}$. The sample studied by Chopelas &
 283 Hofmeister [78] had an x value much comparable to our N-Sp, so that a weak peak
 284 at $\sim 222 \text{ cm}^{-1}$ should be expected. Chopelas & Hofmeister [78], however, did not
 285 report any Raman data below $\sim 250 \text{ cm}^{-1}$.



286

287 **Figure 4.** Raman features of Si-free N-Sp, and synthetic Si-free $\text{MgAl}_2\text{O}_4\text{-Sp}$ from
 288 LMD487.

289

290 In-situ high- T Raman spectroscopic investigations on natural $\text{MgAl}_2\text{O}_4\text{-Sp}$ were
 291 conducted by Cynn et al. [49,86], Van Minh & Yang [87], and Slotznick & Shim [57].
 292 The weak peak at $\sim 715 \text{ cm}^{-1}$ evidently emerged or intensified at high T , and
 293 persisted to ambient T after cooling, so that it could be confidently attributed to the
 294 high- T structural disorder process. Theoretical investigations have confirmed this
 295 attribution [81,83]. In comparison, the even weaker Raman peak at $\sim 222 \text{ cm}^{-1}$ was
 296 detected at high T by Slotznick & Shim [57] only, and similarly attributed to the
 297 high- T structural disorder process. Additionally, it was observed by Cynn et al. [86]
 298 on the natural $\text{MgAl}_2\text{O}_4\text{-Sp}$ after rather than before their high- T Raman
 299 spectroscopic experiments.

300 The two Raman peaks at ~ 222 and 715 cm^{-1} directly observed on our N-Sp ($x =$
 301 ~ 0.145) may provide a convenient and inexpensive method to quantify the disorder
 302 extent of natural 2-3 Sp. Recording rich genetic conditions such as chemical
 303 environment, geological setting, and cooling history [77,88], natural 2-3 Sp
 304 commonly have x values ranging from 0 to ~ 0.23 ([89]; and references therein). The
 305 x parameters are usually constrained by applying single-crystal XRD method,
 306 powder neutron diffraction or nuclear magnetic resonance spectroscopy, which is
 307 often instrumentally unavailable, technically challenging, requires large quantity of

homogeneous sample, and/or costs too much in terms of funds and time. Raman spectroscopy is however right to the opposite. The Raman feature at $\sim 715\text{ cm}^{-1}$ has high intensity, and is well separated from the A_{1g} band at $\sim 766\text{ cm}^{-1}$, so that it can be readily used to estimate the disorder extent (Fig. 4). With fixed analytical conditions in the Raman spectroscopic experiments, the intensity ratio of these two peaks should reflect the inversion extent according to the following equation [86]:

$$x = 1/[1 + c(I_{715}/I_{766})] \quad (3),$$

where c is an unknown coefficient presumably dependent to the analytical setups, and I represents either the peak height or integrated area. With the peak height data (or integrated area data) of our N-Sp, $I_{715} = 1672(437)$ and $I_{766} = 30257(548)$ cps (or $I_{715} = 22995(5993)$ and $I_{766} = 664010(7038)$ cps cm^{-1}), c is estimated as 0.33(9) (or 0.20(6)). Applying this value to the Raman data of the unannealed natural MgAl_2O_4 -Sp of Cynn et al. [86] leads to an x value of ~ 0.06 (or 0.09). Cynn et al. [86] obtained $x = 0.02$ by assuming $c = 1$. We prefer the larger x value, simply because a disorder extent of 0.02 in the MgAl_2O_4 -Sp structure may not be high enough to bring forth the Raman peak at $\sim 715\text{ cm}^{-1}$.

3.3 Mg-Al order-disorder state of synthetic MgAl_2O_4 -Sp

The Mg-Al order-disorder states of our synthetic MgAl_2O_4 -Sp can be estimated using the results from the in-situ observations at high P - T conditions made by Méducin et al. [45], as shown in Fig. 5.

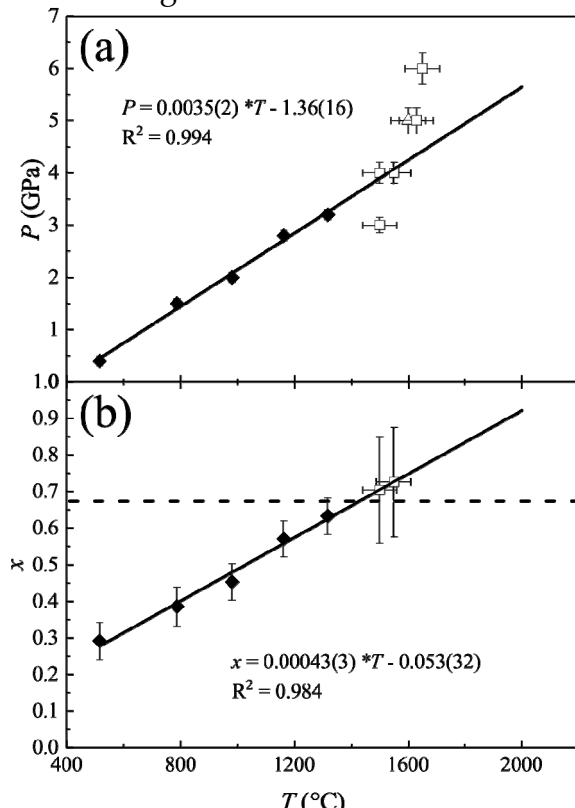


Figure 5. (a) Comparison of P - T conditions of our high- P Sp-synthesizing experiments and those of the heating-up experiments closely approaching Mg-Al

331 redistribution equilibrium at $T \geq 500$ °C from Méducin et al. [45]. The P and T values
332 of the five experiments from Méducin et al. [45] were highly correlated, as shown
333 by the solid line $P = 0.0035(2)*T - 1.36(16)$. (b) x - T relation of those five experiments
334 from Méducin et al. [45], as shown by the solid line $x = 0.00043(3)*T - 0.053(32)$.
335 Filled diamonds are for the five experiments from Méducin et al. [45], whereas
336 empty triangle is for our experiment synthesizing Si-free MgAl_2O_4 -Sp and empty
337 squares are for our experiments synthesizing Si-bearing MgAl_2O_4 -Sp. The broken
338 line in (b) is shown for a hypothetic fully-disordered MgAl_2O_4 -Sp with $x = 0.667$.
339

340 There has been excellent agreement on the T effect on the Mg-Al disorder
341 process of the MgAl_2O_4 -Sp at ambient P : x increases as T increases
342 [42,47,48,50,51,53-57]. As to the P effect at ambient T , discrepancy exists presumably
343 because the order-disorder reaction could not be readily activated and adequately
344 approach its equilibrium during the course of a conventional high- P study
345 [52,90,91]. Thanks to Méducin et al. [45] who conducted an investigation at
346 simultaneously high- P and high- T conditions (up to 3.2 GPa and 1318 °C), the P
347 effect at relatively high T has been well established: x increases as P increases. It is
348 thus clear that our synthetic MgAl_2O_4 -Sp formed at high P - T conditions should
349 attain large degrees of cation disorder, which should be well preserved due to the
350 quick quench process in the cubic press experiments (T decreased to < 600 °C in ~20
351 seconds).

352 Claimed by Méducin et al. [45], the heating-up experiments at $T \geq 500$ °C closely
353 reached their cation order-disorder equilibrium, with the P almost linearly
354 correlating with the T (Fig. 5a). Since both P and T promote Mg-Al disorder at
355 simultaneously high- P and high- T conditions, the effects of P and T can be lumped
356 together and adequately accounted for by using just one independent variable.
357 Here we have chosen T (Fig. 5b). Coincidentally, our synthesizing experiments at 4
358 GPa and 1500 to 1550 °C (Table 1) plot rather near the P - T locus defined by those
359 heating-up experiments at $T \geq 500$ °C (Fig. 5a), suggesting that, with a short-distance
360 extrapolation, the x values of the MgAl_2O_4 -Sp from our experiments at 4 GPa can be
361 accurately estimated. Using the equation shown in Fig. 5b, the derived x values are
362 from 0.70(15) to 0.73(15), so that the true x values should be close to 0.667 (random
363 Mg-Al distribution). In addition, the x values of our synthetic MgAl_2O_4 -Sp at 5 and
364 6 GPa should also be ~0.667 due to the even higher experimental P and T (Fig. 5a).
365 Furthermore, the x values obtained for the P - T conditions of 2.8 GPa and 1163 °C,
366 and 3.2 GPa and 1318 °C by Méducin et al. (2004) were 0.571(49) and 0.633(50),
367 respectively, implying that the x of our MgAl_2O_4 -Sp at a similar P of 3 GPa but a
368 much higher T of 1500 °C (LMD565; Table 1) should be close to 0.667 as well.

369 Assuming no effect of the additional Si with abundances $\leq \sim 0.025$ pfu (Fig. 3),
370 we conclude that our synthetic MgAl_2O_4 -Sp should achieve a nearly random Mg-Al
371 distribution.

372

373

374 **3.4 Raman features of fully-disordered MgAl₂O₄-Sp**

375 The Raman spectrum of our synthetic Si-free MgAl₂O₄-Sp (LMD487) is
376 compared to that of our N-Sp in Fig. 4. It similarly shows six peaks at slightly
377 different energies, with all peaks being significantly broadened though. Compatible
378 with the observations made by Cynn et al. [49,86] and Slotznick & Shim [57], the A_{1g},
379 E_g and T_{2g(1)} modes shift slightly to lower wavenumbers whereas the T_{2g(2)} mode
380 shifts slightly to higher wavenumbers, as x increases from ~0.145 to 0.667. In
381 addition, the E_g band becomes not only very broad, but highly asymmetric as well,
382 indicating a possible hiding Raman peak. According to Caracas & Banigan [84], a
383 very intense Raman feature should occur at the lower wavenumber side of the E_g
384 peak when the MgAl₂O₄-Sp disorders. Moreover, the two weak, broad, and Mg-Al
385 disorder-related peaks at ~715 and 222 cm⁻¹ become much more distinct in the
386 Raman spectrum of the synthetic Si-free MgAl₂O₄-Sp. All these are diagnostic
387 features for a high degree of Mg-Al disorder.

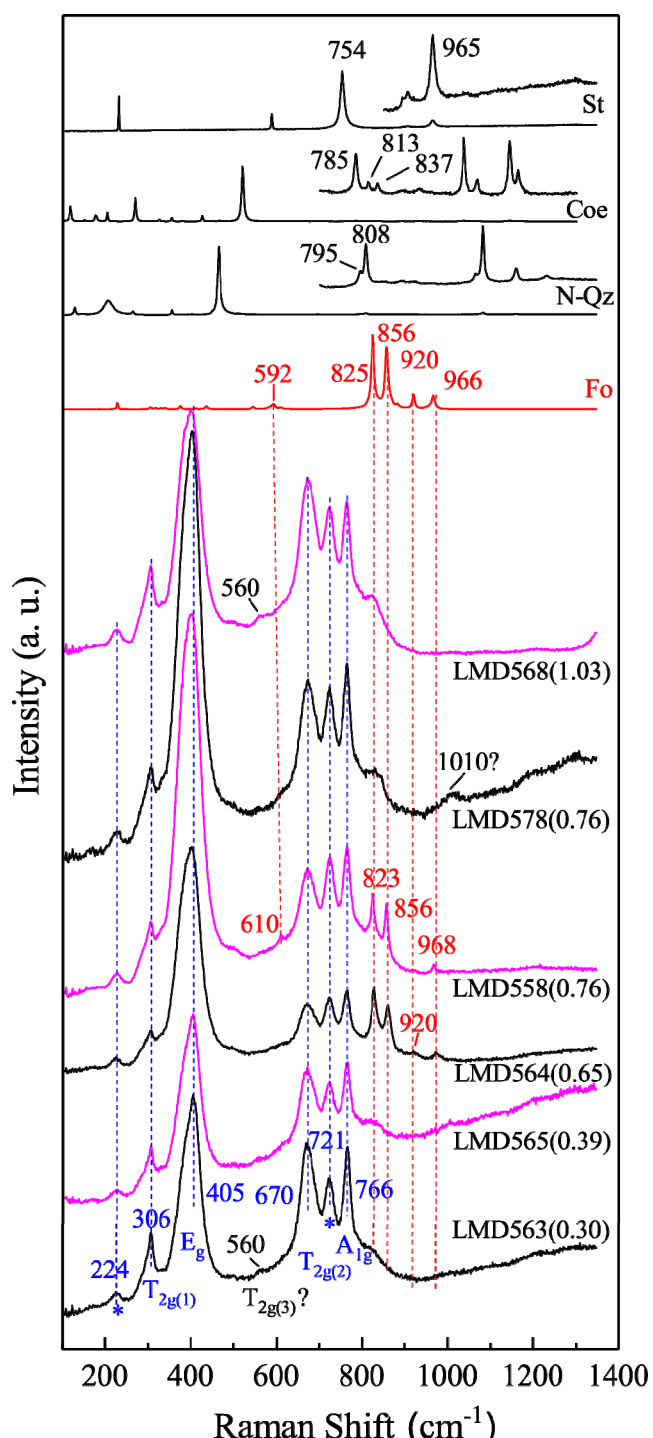
388 With Equation (3) and adopting $x = 0.667$, the peak height data (or integrated
389 area data) of our synthetic Si-free MgAl₂O₄-Sp, $I_{723} = 7148(215)$ and $I_{765} = 10986(228)$
390 cps (or $I_{723} = 181810(5451)$ and $I_{765} = 240020(6329)$ cps cm⁻¹), lead to a c value as 0.32(2)
391 (or 0.38(2)), which is again much smaller than the assumed value of 1 in Cynn et al.
392 [86]. Combining this result with that determined by the Raman data of our N-Sp,
393 0.33(9) or 0.20(6), the c coefficient appears generally constant for a large range of x ,
394 supporting the constant c assumption made by Cynn et al. [86]. To confirm this,
395 more investigation on the MgAl₂O₄-Sp with different disorder extents using jointed
396 experimental methods to simultaneously obtain Raman spectroscopic data,
397 chemical compositional data and crystal structural data like what we have done in
398 this study is highly desirable.

399 **3.5 Raman features of Si-bearing fully-disordered MgAl₂O₄-Sp**

400 The octahedra in the Sp structure share six edges with six neighboring
401 octahedra, resulting in an extensively edge-linked structure in three dimensions
402 [92]. In comparison, the tetrahedra are fully isolated to each other, with their four
403 oxygen atoms linking to four neighboring octahedra. If Si occupied the M-site of the
404 MgAl₂O₄-Sp, its Raman signals would be much analogous to those of St, which
405 similarly places Si in edge-shared octahedra [93]. If Si occupied the T-site,
406 alternatively, its Raman signals would resemble those of Fo because Si in Fo also
407 adopts isolated T-site and forms separate SiO₄ group, with the oxygen atoms shared
408 by neighboring octahedral [94]. On the other hand, Si atoms in low Qz [95] and Coe
409 [96] are 4-coordinated, but the SiO₄ tetrahedra are fully polymerized into a
410 three-dimensional framework, so that the Raman features of low Qz and Coe
411 should be very different to those of potential SiO₄ groups in the Sp structure.

412 Apart from those six bands previously described, the Si-bearing MgAl₂O₄-Sp
413 shows a new set of well-defined Raman bands at ~610, 823, 856 and 968 cm⁻¹ (Fig. 6).
414 These peaks are distinctly different to the Raman features of St, Coe and N-Qz, but
415 highly resemble those of Fo. Furthermore, a less well-defined peak with low

416 intensity occasionally appears at $\sim 920\text{ cm}^{-1}$, and perfectly matches the relatively
 417 weak 920 cm^{-1} Raman peak of Fo (Fig. 6). Accordingly, we tend to attribute these
 418 five peaks to potential separate SiO_4 groups in our Si-bearing, fully Mg-Al
 419 disordered $\text{MgAl}_2\text{O}_4\text{-Sp}$, and assign the peaks at ~ 968 , 920 and 856 cm^{-1} to the
 420 asymmetric stretching of the SiO_4 groups, the peak at $\sim 823\text{ cm}^{-1}$ to the symmetric
 421 stretching, and the peak at $\sim 610\text{ cm}^{-1}$ to the bending. It follows that at least some Si
 422 atoms adopt the T-site.



423

424 **Figure 6.** Raman features of synthetic Si-bearing $\text{MgAl}_2\text{O}_4\text{-Sp}$ from our high- P
 425 experiments. As comparisons, Raman spectra of N-Qz, synthetic Coe, St and Fo

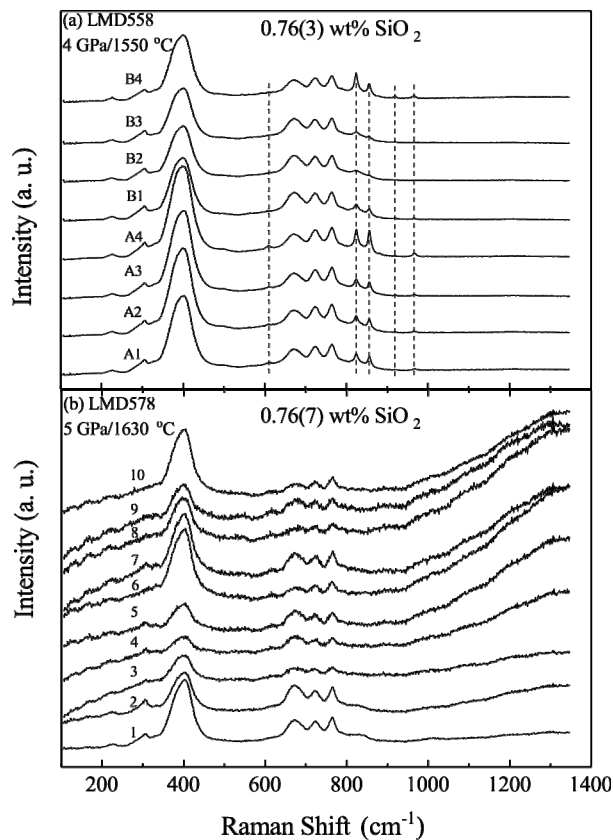
426 (LMD558; Table 1) are shown as well. For the purpose of illustration, some portions
427 of the Raman spectra of St, Coe and N-Qz have been expanded and shown as insets
428 whereas the entire Raman spectrum of Fo has been compressed by a factor of 60.
429 LMD563(0.30), Exp. # followed by the SiO₂ content of the Sp. To illustrate clearly,
430 only one Raman spectrum is shown for each synthetic phase, although multiple
431 Raman spectra have been collected.

432

433 Furthermore, two weak and diffusive Raman peaks have been occasionally
434 observed at ~560 and 1010 cm⁻¹ for our Si-bearing MgAl₂O₄-Sp (Fig. 6), with the
435 former attributable to the usually-undetected fifth fundamental Raman band of the
436 MgAl₂O₄-Sp (T_{2g(3)}) and the latter likely featured as a combination band/overtone.

437 The intensities of the Raman peaks attributable to the SiO₄ groups show
438 interesting behavior. Considering the very low SiO₂ contents in the MgAl₂O₄-Sp
439 from LMD563 and LMD565 (0.30(7) wt% and 0.39(5) wt%, respectively; Table 1), the
440 low intensities of the new Raman peaks at ~610, 823, 856 and 968 cm⁻¹ can be readily
441 explained by the small amounts of the SiO₄ group (Fig. 6). As the SiO₂ contents
442 increase, one would anticipate these peaks to grow if some of the added Si entered
443 the T-site. Surprisingly, the Raman spectra of our MgAl₂O₄-Sp with higher SiO₂
444 contents, from 0.65(7) to 1.03(7) wt%, show distinctly divergent behaviors (Fig. 6),
445 with the new Raman peaks at ~610, 823, 856 and 968 cm⁻¹ intensifying for the
446 MgAl₂O₄-Sp synthesized at relatively low *P-T* conditions (4 GPa and 1500 °C for
447 LMD564, and 4 GPa and 1550 °C for LMD558; Table 1) but increasing little for the
448 MgAl₂O₄-Sp synthesized at relatively high *P-T* conditions (5 GPa and 1630 °C for
449 LMD578, and 6 GPa and 1650 °C for LMD568). Evidently, some of the Si atoms
450 added into the MgAl₂O₄-Sp did take the T-site at relatively low *P-T* conditions, but
451 most them did not at relatively high *P-T* conditions. It follows that some Si atoms in
452 the MgAl₂O₄-Sp from LMD578 and LMD568 must have adopted the M-site and
453 formed SiO₆ groups (Fig. 6).

454 The SiO₆ groups seem Raman-inactive. With similar amounts of SiO₂, the
455 MgAl₂O₄-Sp from LMD558 shows much stronger Raman peaks for its SiO₄ groups
456 than that from LMD578 (Fig. 7), suggesting that the former generally contains more
457 SiO₄ groups, but the latter contains more SiO₆ groups. In both cases, no new Raman
458 peaks can be confidently identified, implying that the SiO₆ groups in the
459 MgAl₂O₄-Sp are by and large Raman-inactive. Different crystallographic
460 orientations unlikely affect this conclusion. As shown in Fig. 7a, the two sets of
461 unpolarized Raman spectra for the MgAl₂O₄-Sp in LMD558 (Set A and Set B), taken
462 from the only crystal shown in Fig. 2a but with crystallographic orientations
463 normal to each other, do display some variations in the intensities of the Raman
464 peaks for the SiO₄ groups, but overall exhibit very similar patterns. Furthermore,
465 the 10 unpolarized Raman spectra taken from 10 randomly-selected MgAl₂O₄-Sp
466 grains in LMD578 do not show much variation in their overall appearance as well
467 (Fig. 7b).



468

469 **Figure 7.** Raman spectra of MgAl₂O₄-Sp with almost identical amounts of SiO₂ from
 470 LMD558 (a) and LMD578 (b). The two sets of Raman spectra (A1, A2, A3 and A4 as
 471 Set A, and B1, B2, B3 and B4 as Set B) shown in (a) were collected from the only Sp
 472 grain shown in Fig. 2a, but with their orientations normal to each other. After
 473 obtaining the Raman spectra of Set A, we reprocessed the sample to make a new
 474 exposure normal to the previous one and then collected the Raman spectra of Set B.
 475 Ten Raman spectra shown in (b) were acquired from ten different Sp grains (see Fig.
 476 2b for the positions). Due to data compression, the weak Raman peaks for the SiO₄
 477 groups of the MgAl₂O₄-Sp from LMD578, visible in Fig. 6, are now barely
 478 discernable in (b).

479

480 3.6 Si-disordering in fully-disordered MgAl₂O₄-Sp

481 In the MgAl₂O₄-Sp with SiO₂ contents as low as ~0.65-0.76 wt%, the Raman
 482 peaks for the minor SiO₄ groups can be as intense as those for the major (Mg,Al)O₄
 483 groups (Fig. 6 and Fig. 7a), so that the relationships among the Raman intensity,
 484 SiO₂ content, Si disorder state and *P-T* condition are worth of further exploration.

485 We can write the formula ^[4](Mg_{0.333}Al_{0.667})^[6](Al_{1.333}Mg_{0.667})O₄ for a Si-free Mg-Al
 486 fully-disordered MgAl₂O₄-Sp ($x = 0.667$). Ignoring the effect of small amounts of Si,
 487 one obtains ^[4](Mg_{0.333}Al_{0.667}Si_y)^[6](Al_{1.333}Mg_{0.667}Si_z)O₄ for the Si-containing Mg-Al
 488 fully-disordered MgAl₂O₄-Sp. The Si disorder state is then defined as $y = [Si_y]/([Si_y] + [Si_z]) = [Si_y]/[Si_{total}]$, with $y = 1$ indicating all Si on the T-site, $y = 0$ all Si on the
 489 M-site, and $y = 0.333$ a Si random distribution. Under certain analytical conditions
 490

491 in the Raman spectroscopic experiments, the intensity of a Raman peak caused by
 492 one type of structural unit i (SiO_4 here) is proportional to its abundance ($[i]$; $[\text{Si}_y]$
 493 here), $I_i = c_i \times [i]$ ([86]; c_i is a constant), leading to

494
$$I_{\text{SiO}_4} = c_{\text{SiO}_4} \times [\text{Si}_y] = c_{\text{SiO}_4} \times y \times ([\text{Si}_y] + [\text{Si}_z]) \quad (4),$$

495 where $[\text{Si}_y] + [\text{Si}_z] = \text{Si}_{\text{total}} = 0.0237 \times \text{SiO}_2 \text{ wt\%}$ for the cases with small amounts of
 496 SiO_2 . With the SiO_4 groups represented by the Raman peaks at ~ 823 and 856 cm^{-1}
 497 and the $(\text{Mg}, \text{Al})\text{O}_4$ groups by those at ~ 725 and 766 cm^{-1} , we obtain

498
$$\frac{I_{\text{SiO}_4}}{I_{(\text{Mg}, \text{Al})\text{O}_4}} = \frac{I_{823} + I_{856}}{I_{725} + I_{766}} = \frac{c_{\text{SiO}_4} \times y \times 0.0237 \times \text{SiO}_2 \text{ wt\%}}{I_{725} + I_{766}} \quad (5).$$

499 The term $\frac{c_{\text{SiO}_4} \times 0.0237}{I_{725} + I_{766}}$ is essentially a constant (C), so that Equation (5) can be
 500 briefed as

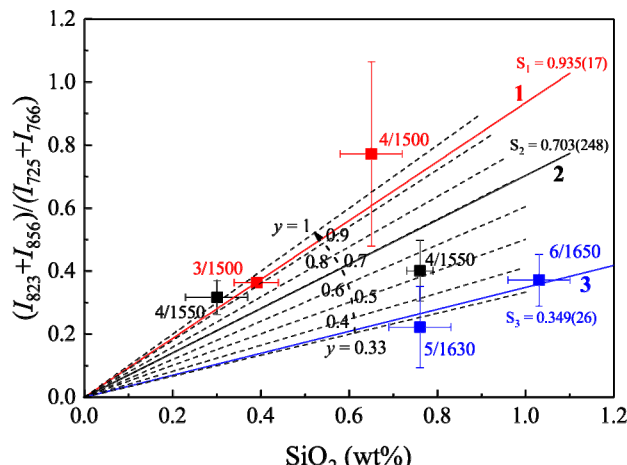
501
$$\frac{I_{823} + I_{856}}{I_{725} + I_{766}} = C \times y \times \text{SiO}_2 \text{ wt\%} \quad (6).$$

502 Evidently, the variable $\frac{I_{823} + I_{856}}{I_{725} + I_{766}}$ of the Mg-Al fully-disordered $\text{MgAl}_2\text{O}_4\text{-Sp}$ with

503 certain y should be linearly correlated with the SiO_2 , and the curve should pass
 504 through the origin (the case of zero SiO_2).

505 Without knowing the y value, it is impossible to obtain the value of the
 506 constant C , which in turn impairs the application of Equation (6). Nevertheless, for
 507 the two extreme cases with all Si entering the T-site ($y = 1$) and Si attaining a full
 508 disorder distribution ($y = 0.333$), the ratio of the two slopes (C and $0.333C$,
 509 respectively) should be 3, which in fact represents the maximum ratio of any two
 510 slopes.

511 Our experimental data are summarized in Table 2, and shown in Fig. 8. Both
 512 LMD563 and LMD558 ran at 4 GPa and $1550 \text{ }^{\circ}\text{C}$, so that they formed a special
 513 group (Group 2) acquiring similar Si order-disorder states (identical y values).
 514 These two experimental data, plus the zero SiO_2 case, then define a curve for this
 515 particular y , with its slope as $S_2 = 0.703(248)$. The uncertainty of the slope is
 516 somehow large, reflecting the limited accuracy of the data.



517

518 **Figure 8.** $\frac{I_{823} + I_{856}}{I_{725} + I_{766}}$ vs SiO₂ content of our synthetic Si-bearing MgAl₂O₄-Sp. Note

that the analytical conditions in the Raman spectroscopic experiments were identical, and all the MgAl₂O₄-Sp generally had the maximum amount of Mg-Al disorder ($x = 0.667$). The experimental P - T conditions are indicated along the symbols; 4/1500, for example, should be read as 4 GPa and 1500 °C. The experiments have been divided into three groups, with Group 1 containing LMD565 and LMD564 (red squares), Group 2 containing LMD563 and LMD558 (black squares), and Group 3 containing LMD578 and LMD568 (blue squares). Aided with the origin (the zero SiO₂ case), the experiments in each group have been used to determine the relationship between the $\frac{I_{823} + I_{856}}{I_{725} + I_{766}}$ and SiO₂ content. Using $C = 1.02(14)$, Equation (6) is shown as the pencil of broken lines radiating from the origin, with different y values ranging from 0.33 to 1.

531 **Table 2.** Ratio of integrated area of the Raman peaks at ~ 823 and 856 cm^{-1} for the SiO_4 group to those
 532 at ~ 725 and 766 cm^{-1} for the $(\text{Mg},\text{Al})\text{O}_4$ group

533	Exp. #	$P/T/\text{SiO}_2^{\text{a}}$	# ^b	$(I_{823}+I_{856})/(I_{725}+I_{766})$
534	LMD565	3/1500/0.39(5) ^c	3	0.36(1)
535	LMD564	4/1500/0.65(7)	3	0.77(29)
536	LMD563	4/1550/0.30(7)	3	0.32(5)
537	LMD558	4/1550/0.76(3)	8	0.40(10)
538	LMD578 ^d	5/1630/0.76(7)	4	0.22(13)
539	LMD568	6/1650/1.03(7)	3	0.37(8)

^a P , GPa; T , °C; SiO_2 , SiO_2 content (wt%) in our synthetic Sp.

541 ^bNumber of Raman spectra collected.

542 ^cNumber in the parenthesis representing one standard

543 deviation; 0.39(5) read as 0.39 ± 0.05 .
544 ^dTen Raman spectra were collected (Fig. 7a), but only four of
545 them were used here. Since the Raman spectra were
546 numerically dominated by those without visible peaks for
547 the SiO_4 groups, we selected four Raman spectra, with the
548 SiO_4 Raman peaks ranging from the lowest to the highest, to
549 derive our result in order to avoid possible data bias. Of
550 course, this procedure might have led to new data bias.

551 The curve constrained by the experiments of Group 2 divides the rest four
552 experiments into two groups, with one group including LMD565 and LMD564
553 conducted at relatively low P - T conditions (Group 1 with larger y) whereas the
554 other group including LMD578 and LMD568 conducted at relatively high P - T
555 conditions (Group 3 with smaller y). Due to the good linear relations (Fig. 8), we
556 have attempted weighted linear least-squares fit and obtained $S_1 = 0.935(17)$ for the
557 experiments of Group 1 and $S_3 = 0.349(26)$ for the experiments of Group 3. The
558 assumption behind this practice is that the y values of the MgAl_2O_4 -Sp from the
559 experiments in either Group 1 or Group 3 are constant. Whether this assumption is
560 justified or not is unimportant, since one can always draw a line through the origin
561 and one single experimental data, and subsequently define a slope for that
562 particular case. The key observation here is that the ratio between S_1 and S_3 is
563 2.68(21), a value close to 3. This means that the curve defined by the experiments of
564 Group 1 generally approximates the case of all Si residing on the T-site ($y = 1$), and
565 the curve defined by the experiments of Group 3 closely approaches the case of a
566 fully random Si distribution ($y = 0.333$). It thus follows that with small variations of
567 P and T , from 3-4 GPa to 5-6 GPa, and from 1500 to 1630-1650 °C, Si in the Mg-Al
568 fully-disordered MgAl_2O_4 -Sp drastically changes from a fully-ordered distribution
569 on the T-site to a completely random distribution.

570 With the y values for the Mg-Al fully-disordered MgAl_2O_4 -Sp from LMD565,
571 LMD564, LMD578 and LMD568, we have calculated the constant C , and obtained
572 0.93(15), 1.19(58), 0.88(59) and 1.08(31), respectively. Indeed, the constant C is
573 constant, averagely 1.02(14), which then allows us to add into Fig. 8 a set of curves
574 with fixed y values to show the relationship between the $\frac{I_{823} + I_{856}}{I_{725} + I_{766}}$ and SiO_2 .

575 Some interesting points emerge from Fig. 8. Firstly, the Raman peaks of the
576 minor SiO_4 group are very prominent, compared to those of the major $(\text{Mg},\text{Al})\text{O}_4$
577 group. For ~1.1 wt% SiO_2 fully-ordered on the T-site ($y = 1$), for example, the
578 Raman peaks at ~823 and 856 cm^{-1} are generally as intense as the Raman peaks at
579 ~725 and 766 cm^{-1} . Secondly, the behavior of the Raman peaks of the SiO_4 group
580 strongly correlates with the SiO_2 content, relatively weak and changing little for the
581 SiO_2 -poor MgAl_2O_4 -Sp but strong and varying significantly for the SiO_2 -rich
582 MgAl_2O_4 -Sp. Thirdly, the Si-disordering process is independent to the SiO_2 content,
583 but controlled by the formation P and T of the MgAl_2O_4 -Sp. With the P - T
584 conditions change from ~3-4 GPa and 1500 °C to ~5-6 GPa and 1630-1650 °C, the Si

585 cations radically change from fully ordering on the T-site ($y = 1$) to randomly
586 distributing between the T-site and M-site ($y = 0.333$). For the $\text{MgAl}_2\text{O}_4\text{-Sp}$ with
587 similar SiO_2 contents, finally, the ones displaying relatively strong Raman peaks at
588 ~ 823 and 856 cm^{-1} should have formed in a relatively low $P\text{-}T$ environment, and
589 vice versa.

590 **4. Implications**

591 Electrostatic lattice energy calculations and consideration of the structure of the
592 Sp group of minerals suggest that the larger Mg cations prefer the T-site and the
593 smaller Al cations prefer the M-site, resulting in a generally normal $\text{MgAl}_2\text{O}_4\text{-Sp}$ at
594 ambient P and T [59]. This principle seems inapplicable to the minor components.
595 The present study indicates that at $P\text{-}T$ conditions $\leq \sim 3\text{-}4 \text{ GPa}$ and $1500 \text{ }^\circ\text{C}$, covering
596 the $P\text{-}T$ range of the top upper mantle of the Earth [97], the even smaller Si cations
597 incorporated by the $\text{MgAl}_2\text{O}_4\text{-Sp}$ structure appear on the T-site, rather than on the
598 anticipated M-site ($y = 1$; Fig. 8). This result is compatible with existing
599 single-crystal XRD studies on terrestrial Sp, which locate Si on the T-site
600 [73,75-77,98]. The current study further shows that presenting as SiO_4 groups in the
601 Sp, a small amount of SiO_2 like $\sim 1 \text{ wt\%}$ exhibits very intense Raman peaks at ~ 823
602 and 856 cm^{-1} , and can completely alter the stereotypical overall appearance of the
603 Raman spectra established with some SiO_2 -poor natural 2-3 Sp. Since Si readily
604 enters the 2-3 Sp structure, this result should have important application in
605 identifying the Sp phase, particularly for the circumstances where direct
606 petrographic observation cannot be made. A Raman spectrometer will be launched
607 shortly as part of the ExoMars analytical laboratory and deployed on the Martian
608 surface to investigate the mineralogical and biological aspects of the Mars [99,100].
609 Considering the wide spreading of the 2-3 Sp on the Earth, the Moon, and the
610 extraterrestrial planets, asteroids and meteorites, it will have high chance to
611 encounter some Sp and collect in-situ Raman spectra. A correct interpretation of
612 these Raman spectra must critically evaluate the effect of Si.

613 Si starts to enter the M-site of the $\text{MgAl}_2\text{O}_4\text{-Sp}$ at $P\text{-}T$ conditions $\geq \sim 3\text{-}4 \text{ GPa}$ and
614 $1500 \text{ }^\circ\text{C}$, and become fully disordered at $P\text{-}T$ conditions $\geq \sim 5\text{-}6 \text{ GPa}$ and $1630\text{-}1650$
615 $^\circ\text{C}$ (Fig. 8). However, the 6-coordinated Si may not be easily observed in natural
616 $\text{MgAl}_2\text{O}_4\text{-Sp}$. High- P experimental studies have showed that Al-rich 2-3 Sp is not a
617 stable phase for the upper mantle at $P > \sim 3 \text{ GPa}$ [101]. On the other hand, adding
618 Cr may stabilize the 2-3 Sp to much higher P [4], and encapsulating the 2-3 Sp in
619 diamonds may lead to the same result [102]. The Cr-rich 2-3 Sp inclusions in
620 diamonds are thus the best targets to look for the 6-coordinated Si.

621 The almost random Si distribution observed for our Si-bearing $\text{MgAl}_2\text{O}_4\text{-Sp}$ at
622 $P\text{-}T$ conditions $\geq \sim 5\text{-}6 \text{ GPa}$ and $1630\text{-}1650 \text{ }^\circ\text{C}$ strongly hints that at some high $P\text{-}T$
623 conditions the Si cations in the $(\text{Mg},\text{Fe})_2\text{SiO}_4\text{-Sp}$ (Rw) might be disordered to large
624 extents. $\text{Mg}_2\text{SiO}_4\text{-Rw}$ has been conventionally regarded as a normal 4-2 spinel with
625 nearly all Si taking the T-site. The single-crystal XRD data of Sasaki et al. [64] and
626 high-resolution ^{29}Si NMR data of Stebbins et al. [61] did not show any convincing

627 evidence for 6-coordinated Si. In contrast, ~4% Si was inferred to appear on the
628 M-site, based on the systematic deviations of the Si-O bond length determined by
629 new single-crystal XRD data from an average value in silicates [60]. Consideration
630 of the bond length systematics and experimentally-measured cation distributions
631 led to a similar conclusion [59]. However, all these conclusions were drawn from
632 the experimental data collected on quenched samples or based on some crystal
633 structural features established for ambient P . In the former cases, the cation
634 disorder information of the Rw at high P might be completely lost. In analogy to the
635 well-known partial preservation of the high- T equilibrium state of the Al-Mg
636 disorder in the MgAl₂O₄-Sp after quenching [42,53], reordering the Si and Mg
637 cations in the Mg₂SiO₄-Sp presumably happens fast and proceeds towards its
638 completion as the high- P synthesizing experiment quenches. In the latter cases, the
639 bond length systematics and structural features established for ambient P might not
640 be applicable to the high- P structures. As pointed out by Méducin et al. [45], P has a
641 significant impact on the order-disorder process of the MgAl₂O₄-Sp, especially in
642 the T range of 477–1227 °C. Some high- P single-crystal XRD investigations have
643 been conducted up to ~28.9 GPa at ambient T , but could not shed light on the Si
644 disorder issue, partially due to the low experimental T potentially unable to trigger
645 the order-disorder reaction, and partially due to the low data resolution caused by
646 the similar X-ray scattering factors of Mg and Si [103,104].

647 The most likely evidences in the literature to the presence of 6-coordinated Si in
648 the Rw came from a high- P Raman spectroscopic investigation on synthetic
649 Mg₂SiO₄-Rw [105] and a spectroscopic study on some meteoritic Rw [62]. At $P > \sim 30$
650 GPa, a weak and diffusive Raman peak appeared and was interpreted as the
651 signature for the presence of Si-O-Si linkages and/or partial increase in the
652 coordination of Si [105]. We propose that this peak might belong to the MgO₄
653 groups in the Mg₂SiO₄-Rw, which would in turn indicate the presence of the SiO₆
654 groups resulted from the position exchange of the Si and Mg cations. According to
655 Chopelas et al. [106], the MgO₆ groups in the normal Mg₂SiO₄-Rw are Raman-silent,
656 and the SiO₄ groups are responsible for all the Raman peaks. Since the
657 order-disorder process in the Sp is non-convergent (i.e., the symmetry of the Sp is
658 maintained at any inversion), no new Raman peaks should be expected from the
659 SiO₆ groups in the disordered Mg₂SiO₄-Rw, exactly like what we have observed for
660 the Si-bearing MgAl₂O₄-Sp (Figs. 6, 7). On the line of the study about the meteoritic
661 Rw, Taran et al. [62] used a range of analytical methods including optical
662 absorption spectroscopy to investigate some synthetic (Mg,Fe)₂SiO₄-Rw, and two
663 compositionally homogenous but doubly-colored meteoritic Rw grains (Grain 1,
664 one part being colorless and the other part blue; Grain 2, one part being blue and
665 the other part dark blue) from two L6-type ordinary chondrites NWA 1662 and
666 NWA 463. They proposed that for the meteoritic Rw, the part with no color was
667 inverse Rw, other parts with various colors were Rw with different amounts of
668 cation inversion. In order to confirm their hypothesis, more investigation should be
669 conducted on the meteoritic Rw, which represent the best natural specimen to
670 study high- P structural features including the Mg-Si order-disorder state due to

671 much larger quench rates. Rw with various colors have been documented in many
672 meteorites such as the L ordinary chondrites [107-111], LL ordinary chondrites
673 [14,26], and Martian meteorites like the shergottites [32,34,37]. If the relationship
674 among the color, composition, inverse magnitude, P and T can be adequately
675 quantified, a fine scale for accurately estimating the shock P - T conditions may be
676 derived, which may serve well the theoretical evolution models of the early solar
677 system.

678 If the Rw in the LP-MTZ attained substantially higher degrees of inverse than
679 those experimentally observed so far, the mineralogical model of the upper mantle
680 and the nature of the 520-km and 620-km seismic discontinuities would need
681 further careful examination. Some empirical and theoretical studies have
682 demonstrated that the cation disorder process in the Rw leads to significantly larger
683 thermal expansion coefficients, smaller bulk modulus, and smaller shear modulus
684 [19,44,46,63]. As a result, a 12.5% Si-Mg disorder can decrease the seismic velocities
685 by ~3-5% [19,46]. Direct experimental investigations on the cation inversion of the
686 Rw at the P - T conditions of the LP-MTZ are therefore of high priority.

687 **Acknowledgements:** This study was financially supported by the Strategic Priority
688 Research Program (B) of Chinese Academy of Sciences (Grant No. XDB18000000),
689 by the DREAM project of MOST, China (Grant No. 2016YFC0600408), and by the
690 Program of the Data Integration and Standardization in the Geological Science and
691 Technology from MOST, China (Grant No. 2013FY1109000-3).

692 **Author Contributions:** Xi Liu (designing the project). Liping Liu (writing the initial
693 draft of the work). Xi Liu (writing the final paper). Xi Liu, Liping Liu and Xinjian
694 Bao (interpreting the results). Liping Liu, Qiang He and Renbiao Tao (conducting
695 high- P experiments). Liping Liu, Wei Yan, Yunlu Ma and Mingyue He (collecting
696 Raman spectra). Xinjian Bao, Liping Liu and Ruqian Zou (collecting and
697 interpreting the single-crystal X-ray data). Liping Liu (performing EMP analyses).
698 Mingyue He (helping in checking the draft of the paper). All authors discussed the
699 results and commented on the manuscript.

700 **Conflicts of Interests:** The authors declare no conflict of interests.

701 **References**

- 702 1. Evans, B.W.; Frost, B.R. Chrome-spinel in progressive metamorphism-a preliminary analysis.
703 *Geochim. Cosmochim. Acta* **1975**, *39*, 959-972.
- 704 2. Barnes, S.J.; Roeder, P.L. The range of spinel compositions in terrestrial mafic and ultramafic
705 rocks. *J. Petrol.* **2001**, *42*, 2279-2302.
- 706 3. Fabries, J. Spinel-olivine geothermometry in peridotites from ultramafic complexes. *Contrib.
707 Mineral. Petrol.* **1979**, *69*, 329-336.
- 708 4. O'Neill, H.St.C. The transition between spinel lherzolite and garnet lherzolite, and its use as a
709 geobarometer. *Contrib. Mineral. Petrol.* **1981**, *77*, 185-194.
- 710 5. Ballhaus, C.; Berry, R.F.; Green, D.H. High pressure experimental calibration of the
711 olivine-orthopyroxene-spinel oxygen barometer: Implications for the oxidation state of the
712 upper mantle. *Contrib. Mineral. Petrol.* **1991**, *107*, 27-40.
- 713 6. Dick, H.J.B.; Bullen, T. Chromian spinel as a petrogenetic indicator in abyssal and alpine-type

714 peridotites and spatially associated lavas. *Contrib. Mineral. Petrol.* **1984**, *86*, 54-76.

715 7. Liang, Y.; Elthon, D. Evidence from chromium abundances in mantle rocks for extraction of
716 picrite and komatiite melts. *Nature* **1990**, *343*, 551-553.

717 8. Liu, X.; O'Neill, H.St.C. The effect of Cr₂O₃ on the partial melting of spinel lherzolite in the
718 system CaO-MgO-Al₂O₃-SiO₂-Cr₂O₃ at 1.1 GPa. *J. Petrol.* **2004**, *45*, 2261-2286.

719 9. Zhang, Y.; Liu, X.; Xiong, Z.; Zhang, Z. Compressional behavior of MgCr₂O₄ spinel from
720 first-principles simulation. *Sci. China Earth Sci.* **2016**, *59*, 989-996.

721 10. Xie, X.; Chen, M.; Wang, D. Shock-related mineralogical features and P-T history of the Suizhou
722 L6 chondrite. *Eur. J. Mineral.* **2001**, *13*, 1177-1190.

723 11. Wang, A.; Kuebler, K.E.; Jolliff, B.L.; Haskin, L.A. Raman spectroscopy of Fe-Ti-Cr-oxides, case
724 study: Martian meteorite EETA 79001. *Am. Mineral.* **2004**, *89*, 665-680.

725 12. Fritz J.; Greshake, A. High-pressure phases in an ultramafic rock from Mars. *Earth Planet. Sci.*
726 *Lett.* **2009**, *288*, 619-623.

727 13. Lenaz, D.; Princivalle, F.; Schmitz, B. First crystal-structure determination of chromites from an
728 acapulcoite and ordinary chondrites. *Mineral. Mag.* **2015**, *79*, 755-765.

729 14. Hu, J.; Sharp, T.G. High-pressure phases in shock-induced melt of the unique highly shocked
730 LL6 chondrite Northwest Africa 757. *Meteorit. Planet. Sc.* **2016**, *51*, 1353-1369.

731 15. Pieters, C.M.; Besse, S.; Boardman, J.; Buratti, B.; Cheek, L.; Clark, R.N.; Combe, J.P.; Dhingra,
732 D.; Goswami, J.N.; Green, R.O.; Head, J.W.; Isaacson, P.; Klima, R.; Kramer, G.; Lundein, S.;
733 Malaret, E.; McCord, T.; Mustard, J.; Nettles, J.; Petro, N.; Runyon, C.; Staid, M.; Sunshine, J.;
734 Taylor, L.A.; Thaisen, K.; Tompkins, S.; Whitten, J. Mg-spinel lithology: A new rock type on the
735 lunar farside. *J. Geophys. Res. Atmo.* **2011**, *116*, 287-296.

736 16. Gross, J.; Treiman, A.H. Unique spinel-rich lithology in lunar meteorite ALHA81005: Origin
737 and possible connection to M³ observations of the farside highlands. *J. Geophys. Res.* **2011**, *116*,
738 E10009.

739 17. Ringwood, A.E. Phase transformations and their bearing on the constitution and dynamics of
740 the mantle. *Geochim. Cosmochim. Acta* **1991**, *55*, 2083-2110.

741 18. Li, B.; Liebermann, R.C. Indoor seismology by probing the Earth's interior by using sound
742 velocity measurements at high pressures and temperatures. *P. Natl. Acad. Sci. USA.* **2007**, *104*,
743 9145-9150.

744 19. Panero, W.R. Cation disorder in ringwoodite and its effects on wave speeds in the Earth's
745 transition zone. *J. Geophys. Res.* **2008**, *113*, B10204.

746 20. Stixrude, L.; Lithgow-Bertelloni, C. Thermodynamics of mantle minerals - II. Phase equilibria.
747 *Geophys. J. Int.* **2011**, *184*, 1180-1213.

748 21. Liu, X.; Xiong, Z.; Chang, L.; He, Q.; Wang, F.; Shieh, S.R.; Wu, C.; Li, B.; Zhang, L. Anhydrous
749 ringwoodites in the mantle transition zone: Their bulk modulus, solid solution behavior,
750 compositional variation, and sound velocity feature. *Solid Earth Sci.* **2016**, *1*, 28-47.

751 22. Pearson, D.G.; Brenker, F.E.; Nestola, F.; McNeill, J.; Nasdala, L.; Hutchison, M.T.; Matveev, S.;
752 Mather, K.; Silversmit, G.; Schmitz, S.; Vekemans, B.; Vincze, L. Hydrous mantle transition zone
753 indicated by ringwoodite included within diamond. *Nature* **2014**, *507*, 221-224.

754 23. Tomioka, N.; Miyahara, M. High-pressure minerals in shocked meteorites. *Meteorit. Planet. Sc.*
755 **2017**, *52*, 2017-2039.

756 24. Chen, M.; Xie, X. The shock effects of olivine in the Yanzhuang chondrite. *Acta Mineral. Sin.*
757 **1993**, *13*, 109-116.

758 25. Kimura, M.; Chen, M.; Yoshida, T.; El Goresy, A.; Ohtani, E. Back-transformation of
759 high-pressure phases in a shock melt vein of an H-chondrite during atmospheric passage:
760 Implications for the survival of high-pressure phases after decompression. *Earth Planet. Sci. Lett.*
761 **2003**, *217*, 141-150.

762 26. Bischoff, A. Discovery of purple-blue ringwoodite within shock veins of an LL6 ordinary
763 chondrite from Northwest Africa. 33rd Lunar and Planetary Science Conference, Houston,
764 2002.

765 27. Hollister, L.S.; Bindi, L.; Yao, N.; Poirier, G.R.; Andronicos, C.L.; MacPherson, G.J.; Lin, C.;
766 Distler, V.V.; Eddy, M.P.; Kostin, A.; Kryachko, V.; Steinhardt, W.M.; Yudovskaya, M.; Eiler, J.M.;

767 Guan, Y.; Clarke, J.J.; Steinhardt, P.J. Impact-induced shock and the formation of natural
768 quasicrystals in the early solar system. *Nat. Commun.* **2014**, *5*, 4040.

769 28. Miyahara, M.; Ohtani, E.; Yamaguchi, A. High-pressure polymorphs in Gujba CB type
770 carbonaceous chondrite. Japan Geoscience Union Meeting, Chiba, 24-28 May 2015; pp. 22-20.

771 29. Barrat, J.A.; Chaussidon, M.; Bohn, M.; Gillet, P.; Göpel, C.; Lesourd, M. Lithium behavior
772 during cooling of a dry basalt: An ion-microprobe study of the lunar meteorite Northwest
773 Africa 479 (NWA 479). *Geochim. Cosmochim. Acta* **2005**, *69*, 5597-5609.

774 30. Zhang, A.; Hsu, W.; Floss, C.; Li, X.; Li, Q.; Liu, Y.; Taylor, L.A. Petrogenesis of lunar meteorite
775 Northwest Africa 2977: Constraints from in situ microprobe results. *Meteorit. Planet. Sc.* **2011**, *45*,
776 1929-1947.

777 31. Boonsue, S.; Spray, J. Shock-induced phase transformations in melt pockets within Martian
778 meteorite NWA 4468. *Spectrosc. Lett.* **2012**, *45*, 127-134.

779 32. Baziotis, I.P.; Yang, L.; Paul, S.; DeCarli, H.; Melosh, J.; McSween, H.Y.; Bodnar, R.J.; Taylor, L.A.
780 The Tissint Martian meteorite as evidence for the largest impact excavation. *Nat. Commun.* **2013**,
781 *4*, 1404.

782 33. Greshake, A.; Fritz, J.; Böttger, U.; Goran, D. Shear-induced ringwoodite formation in the
783 Martian shergottite Dar al Gani 670. *Earth Planet. Sci. Lett.* **2013**, *375*, 383-394.

784 34. Walton, E.L. Shock metamorphism of Elephant Moraine A79001: Implications for
785 olivine-ringwoodite transformation and the complex thermal history of heavily shocked
786 Martian meteorites. *Geochim. Cosmochim. Acta* **2013**, *107*, 299-315.

787 35. Walton, E.L.; Sharp, T.G.; Hu, J.; Filiberto, J. Heterogeneous mineral assemblages in Martian
788 meteorite Tissint as a result of a recent small impact event on Mars. *Geochim. Cosmochim. Acta*
789 **2014**, *140*, 334-348.

790 36. Ma, C.; Tschauner, O.; Beckett, J.R.; Liu, Y.; Rossman, G.R.; Zhuravlev, K.; Prakapenka, V.; Dera,
791 P.; Taylor, L.A. Tissintite, $(\text{Ca}, \text{Na}, \square)\text{AlSi}_2\text{O}_6$, a highly-defective, shock-induced, high-pressure
792 clinopyroxene in the Tissint Martian meteorite. *Earth Planet. Sci. Lett.* **2015**, *422*, 194-205.

793 37. Ma, C.; Tschauner, O.; Beckett, J.R.; Liu, Y.; Rossman, G.R.; Sinogeikin, S.V.; Smith, J.S.; Taylor,
794 L.A. Ahrensite, $\gamma\text{-Fe}_2\text{SiO}_4$, a new shock-metamorphic mineral from the Tissint meteorite:
795 Implications for the Tissint shock event on Mars. *Geochim. Cosmochim. Acta* **2016**, *184*, 240-256.

796 38. Miyahara, M.; Ohtani, E.; El Goresy, A.; Ozawa, S.; Gillet, P. Phase transition processes of
797 olivine in the shocked Martian meteorite Tissint: Clues to origin of ringwoodite-, bridgmanite-
798 and magnesiowüstite-bearing assemblages. *Phys. Earth Planet. In.* **2016**, *259*, 18-28.

799 39. Stöffler, D.; Keil, K.; Scott, E.R.D. Shock metamorphism of ordinary chondrites. *Geochim.
800 Cosmochim. Acta* **1991**, *55*, 3845-3867.

801 40. Chen, M.; Sharp, T.G.; El Goresy, A.; Wopenka, B.; Xie, X. The majorite-pyrope +
802 magnesiowüstite assemblage: Constraints on the history of shock veins in chondrites. *Science*,
803 **1996**, *271*, 1570-1573.

804 41. Sharp, T.G.; DeCarli, P.S. Shock effects in meteorites. In *Meteorites and the early solar system II*;
805 Lauretta, D.S., McSween, H.Y., Eds.; The University of Arizona Press: Tuscon, Arizona, USA,
806 2006; pp. 653-677.

807 42. Wood, B.J.; Kirkpatrick, R.J.; Montez, B. Order-disorder phenomena in MgAl_2O_4 spinel. *Am.
808 Mineral.* **1986**, *71*, 999-1006.

809 43. Hazen, R.M.; Navrotsky, A. Effects of pressure on order-disorder reactions. *Am. Mineral.* **1996**,
810 *81*, 1021-1035.

811 44. Hazen, R.M.; Yang, H. Effects of cation substitution and order-disorder on P-V-T equations of
812 state of cubic spinels. *Am. Mineral.* **1999**, *84*, 1956-1960.

813 45. Méducin, F.; Redfern, S.A.T.; Godec, Y.L.; Stone, H.J.; Tucker, M.G.; Dove, M.T.; Marshall, W.G.
814 Study of cation order-disorder in MgAl_2O_4 spinel by in situ neutron diffraction up to 1600 K
815 and 3.2 GPa. *Am. Mineral.* **2004**, *89*, 981-986.

816 46. Li, L.; Carrez, P.; Weidner, D. Effect of cation ordering and pressure on spinel elasticity by ab
817 initio simulation. *Am. Mineral.* **2007**, *92*, 174-178.

818 47. Schmocker, U.; Waldner, F. The inversion parameter with respect to the space group of
819 MgAl_2O_4 spinels. *J. Phys. C* **1976**, *9*, L235-L237.

820 48. Peterson, R.C.; Lager, G.A.; Hitterman, R.L. A time-of-flight neutron powder diffraction study
821 of MgAl_2O_4 at temperatures up to 1273 K. *Am. Mineral.* **1991**, *76*, 172-180.

822 49. Cynn, H.; Sharma, S.K.; Cooney, T.F.; Nicol, M. High-temperature Raman investigation of
823 order-disorder behavior in the MgAl_2O_4 spinel. *Phys. Rev. B* **1992**, *45*, 500-502.

824 50. Millard, R.L.; Peterson, R.C.; Hunter, B.K. Temperature dependence of cation disorder in
825 MgAl_2O_4 spinel using ^{27}Al and ^{17}O magic-angle spinning NMR. *Am. Mineral.* **1992**, *77*, 44-52.

826 51. Maekawa, H.; Kato, S.; Kawamura, K.; Yokokawa, T. Cation mixing in natural MgAl_2O_4 spinel:
827 A high-temperature ^{27}Al NMR study. *Am. Mineral.* **1997**, *82*, 1125-1132.

828 52. Pavese, A.; Artioli, G.; Hull, S. In situ powder neutron diffraction of cation partitioning vs.
829 pressure in $\text{Mg}_{0.94}\text{Al}_{2.04}\text{O}_4$ synthetic spinel. *Am. Mineral.* **1999**, *84*, 905-912.

830 53. Redfern, S.A.T.; Harrison, R.J.; O'Neill, H.St.C.; Wood, D.R.R. Thermodynamics and kinetics of
831 cation ordering in MgAl_2O_4 spinel up to 1600 °C from in situ neutron diffraction. *Am. Mineral.*
832 **1999**, *84*, 299-310.

833 54. Andreozzi, G.B.; Princivalle, F.; Skogby, H.; Della Giusta, A. Cation ordering and structural
834 variations with temperature in MgAl_2O_4 spinel: An X-ray single-crystal study. *Am. Mineral.*
835 **2000**, *85*, 1164-1171.

836 55. Andreozzi, G.B.; Princivalle, F. Kinetics of cation ordering in synthetic MgAl_2O_4 spinel. *Am.*
837 *Mineral.* **2002**, *87*, 838-844.

838 56. Carbonin, S.; Martignago, F.; Menegazzo, G.; Nal Negro, A. X-ray single-crystal study of
839 spinels: In situ heating. *Phys. Chem. Miner.* **2002**, *29*, 503-514.

840 57. Slotznick, S.P.; Shim, S.H. In situ Raman spectroscopy measurements of MgAl_2O_4 spinel up to
841 1400 °C. *Am. Mineral.* **2008**, *93*, 470-476.

842 58. Sreeja, V.; Smitha, T.S.; Nand, D.; Ajithkumar, T.G.; Joy, P.A. Size dependent coordination
843 behavior and cation distribution in MgAl_2O_4 nanoparticles from ^{27}Al solid state NMR studies. *J.*
844 *Phys. Chem. C* **2008**, *112*, 14737-14744.

845 59. O'Neill, H.St.C.; Navrotsky, A. Simple spinels: Crystallographic parameters, cation radii, lattice
846 energies, and cation distribution. *Am. Mineral.* **1983**, *68*, 181-194.

847 60. Hazen, R.M.; Downs, R.T.; Finger, L.W.; Ko, J. Crystal chemistry of ferromagnesian silicate
848 spinels: Evidence for Mg-Si disorder. *Am. Mineral.* **1993**, *78*, 1320-1323.

849 61. Stebbins, J.F.; Panero, W.R.; Smyth, J.R.; Frost, D.J. Forsterite, wadsleyite, and ringwoodite
850 (Mg_2SiO_4): ^{29}Si NMR constraints on structural disorder and effects of paramagnetic impurity
851 ions. *Am. Mineral.* **2009**, *94*, 626-629.

852 62. Taran, M.N.; Koch-Müller, M.; Wirth, R.; Abs-Wurmbach, I.; Rhede, D.; Greshake, A.
853 Spectroscopic studies of synthetic and natural ringwoodite, γ -(Mg, Fe) $_2\text{SiO}_4$. *Phys. Chem. Miner.*
854 **2009**, *36*, 217-232.

855 63. Kiefer, B.; Stixrude, L.; Wentzcovitch, R. Normal and inverse ringwoodite at high pressures. *Am.*
856 *Mineral.* **1999**, *84*, 288-293.

857 64. Sasaki, S.; Prewitt, C.T.; Sato, Y.; Ito, E. Single crystal x-ray study of γ - Mg_2SiO_4 . *J. Geophys. Res.*
858 **1982**, *87*, 7829-7832.

859 65. Sigurdsson, I.A.; Kamenetsky, V.S.; Crawford, A.J.; Eggins, S.M.; Zlobin, S.K. Primitive island
860 arc and oceanic lavas from the hunter ridge-hunter fracture zone. Evidence from glass, olivine
861 and spinel compositions. *Miner. Petrol.* **1993**, *47*, 149-169.

862 66. Sobolev, A.V.; Nikogosian, I.K. Petrology of long-lived mantle plume magmatism: Hawaii,
863 Pacific and Reunion Island, Indian Ocean. *Petrology* **1994**, *2*, 111-144.

864 67. Kamenetsky, V.S.; Sobolev, A.V.; Joron, J.L.; Semet, M.P. Petrology and geochemistry of
865 cretaceous ultramafic volcanics from eastern Kamchatka. *J. Petrology* **1995**, *36*, 637-662.

866 68. Franz, L.; Wirth, R. Spinel inclusions in olivine of peridotite xenoliths from TUBAF seamount
867 (Bismarck Archipelago/Papua New Guinea): Evidence for the thermal and tectonic evolution of
868 the oceanic lithosphere. *Contrib. Mineral. Petrology* **2000**, *140*, 283-295.

869 69. Chistyakova, S.; Latypov, R.; Zaccarini, F. Chromitite dykes in the Monchegorsk layered
870 intrusion, Russia: In situ crystallization from chromite-saturated magma flowing in conduits. *J.*
871 *Petrology* **2016**, *56*, 2395-2424.

872 70. Liu, X.; Chen, J.; Tang, J.; He, Q.; Li, S.; Peng, F.; He, D.; Zhang, L.; Fei, Y. A large volume cubic

873 press with a pressure-generating capability up to about 10 GPa. *High Pressure Res.* **2012**, *32*,
874 239-254.

875 71. Bertka, C.M.; Fei, Y.W. Mineralogy of the Martian interior up to core-mantle boundary pressure.
876 *J. Geophys. Res.* **1997**, *102*, 5251-5264.

877 72. He, Q.; Tang, J.; Wang, F.; Liu, X. High temperature stable assembly designed for cubic press.
878 *Chin. J. High Pressure Phys.* **2014**, *28*, 145-151.

879 73. Carbonin, S.; Russo, U.; Della Giusta, A. Cation distribution in some natural spinels from X-ray
880 diffraction and Mössbauer spectroscopy. *Mineral. Mag.* **1996**, *60*, 355-368.

881 74. Lavina, B.; Salvialo, G.; Della Giusta, A. Cation distribution and structural modeling of spinel
882 solid solutions. *Phys. Chem. Miner.* **2002**, *29*, 10-18.

883 75. Princivalle, F.; Della Giusta, A.; Carbonin, S. Comparative crystal-chemistry of spinels from
884 some suites of ultramafic rocks. *Miner. Petrol.* **1989**, *40*, 117-126.

885 76. Della Giusta, A.; Carbonin, S.; Ottonello, G. Temperature-dependent disorder in a natural
886 Mg-Al-Fe²⁺-Fe³⁺-spinel. *Mineral. Mag.* **1996**, *60*, 603-616.

887 77. Uchida, H.; Lavina, B.; Downs, R.T.; Chesley, J. Single-crystal X-ray diffraction of spinels from
888 San Carlos volcanic field, Arizona: Spinel as a geothermometer. *Am. Mineral.* **2005**, *90*,
889 1900-1908.

890 78. Chopelas, A.; Hofmeister, A.M. Vibrational spectroscopy of aluminate spinels at 1 atm and of
891 MgAl₂O₄ to over 200 kbar. *Phys. Chem. Miner.* **1991**, *18*, 279-293.

892 79. Lauwers, H.A.; Herman, M.A. Force field of some AB₂C₄ spinel compounds. *J. Phys. Chem.*
893 *Solids* **1980**, *41*, 223-230.

894 80. Sinha, M.M.; Singh, N.P.; Prasad, K.; Gupta, H.C. Effect of rattling on the interatomic interaction
895 in oxide spinels MgAl₂O₄ and ZnGa₂O₄. *Phys. Status Solidi B* **1995**, *190*, K27-K29.

896 81. de Wijs, G.A.; Fang, C.M.; Kresse, G.; de With, G. First-principles calculation of the phonon
897 spectrum of MgAl₂O₄ spinel. *Phys. Rev. B* **2002**, *65*, 094305.

898 82. Thibaudeau, P.; Gervais, F. Ab initio investigation of phonon modes in the MgAl₂O₄ spinel. *J.*
899 *Phys.: Condens. Matter* **2002**, *14*, 3543-3552.

900 83. Lazzeri, M.; Thibaudeau, P. Ab initio Raman spectrum of the normal and disordered MgAl₂O₄
901 spinel. *Phys. Rev. B* **2006**, *74*, 2952-2961.

902 84. Caracas, R.; Banigan, E.J. Elasticity and Raman and infrared spectra of MgAl₂O₄ spinel from
903 density functional perturbation theory. *Phys. Earth Planet. In.* **2009**, *174*, 113-121.

904 85. Kushwaha, A.K. Vibrational and elastic properties of aluminate spinel MgAl₂O₄. *Physica B* **2010**,
905 405, 2795-2798.

906 86. Cynn, H.; Anderson, O.L.; Nicol, M. Effects of cation disordering in a natural MgAl₂O₄ spinel
907 observed by rectangular parallelepiped ultrasonic resonance and Raman measurements. *Pure*
908 *Appl. Geophys.* **1993**, *141*, 415-444.

909 87. Van Minh, N.; Yang, I.-S. A Raman study of cation-disorder transition temperature of natural
910 MgAl₂O₄ spinel. *Vib. Spectrosc.* **2004**, *35*, 93-96.

911 88. Lenaz, D.; Musco, M.E.; Petrelli, M.; Caldeira, R.; Min, A.D.; Marzoli, A.; Mata, J.; Perugini, D.;
912 Princivalle, F.; Boumehdi, M.A.; Bensaid, I.A.A.; Youbi, N. Restitic or not? Insights from trace
913 element content and crystal-structure of spinels in African mantle xenoliths. *Lithos* **2017**,
914 278-281, 464-476.

915 89. Lucchesi, S.; Della Giusta, A. Crystal chemistry of a highly disordered Mg-Al natural spinel.
916 *Miner. Petrol.* **1997**, *59*, 91-99.

917 90. Levy, D.; Pavese, A.; Hanfland, M. Synthetic MgAl₂O₄ (spinel) at high-pressure conditions
918 (0.0001-30 GPa): A synchrotron X-ray powder diffraction study. *Am. Mineral.* **2003**, *88*, 93-98.

919 91. Nestola, F.; Ballaran, T.B.; Zunic, T.B.; Princivalle, F.; Secco, L.; Negro, A.D. Comparative
920 compressibility and structural behavior of spinel MgAl₂O₄ at high pressures: The
921 independency on the degree of cation order. *Am. Mineral.* **2007**, *92*, 1838-1843.

922 92. Bacon, G.E. A neutron-diffraction study of magnesium aluminium oxide. *Acta Crystallogr.* **1952**,
923 5, 684-686.

924 93. Sinclair, W.; Ringwood, A.E. Single crystal analysis of the structure of stishovite. *Nature* **1978**,
925 272, 714-715.

926 94. Smyth, J.R.; Hazen, R.M. The crystal structures of forsterite and hortonolite at several
927 temperatures up to 900 °C. *Am. Mineral.* **1973**, *58*, 588-593.

928 95. Gibbs, R.E. Structure of α quartz. *P. Roy. Soc. A* **1926**, *110*, 443-455.

929 96. Zoltai, T.; Buerger, M.J. The crystal structure of coesite, the dense, high-pressure form of silica.
930 *Z. Kristallogr.* **1959**, *111*, 129-141.

931 97. Katsura, T.; Yamada, H.; Nishikawa, O.; Song, M.; Kubo, A.; Shinmei, T.; Yokoshi, S.; Aizawa, Y.;
932 Yoshino, T.; Walter, M.J.; Ito, E.; Funakoshi, K.-I. Olivine-wadsleyite transition in the system
933 (Mg,Fe)₂SiO₄. *J. Geophys. Res.* **2004**, *109*, B02209.

934 98. Perinelli, C.; Bosi, F.; Andreozzi, G.B.; Conte, A.M.; Armienti, P. Geothermometric study of
935 Cr-spinels of peridotite mantle xenoliths from northern Victoria Land (Antarctica). *Am. Mineral.*
936 **2014**, *99*, 839-846.

937 99. Edwards, H.G.M.; Hutchinson, I.; Ingle, R. The ExoMars Raman spectrometer and
938 identification of biogeological spectroscopic signatures using a flight-like prototype. *Anal.
939 Bioanal. Chem.* **2012**, *404*, 1723-1731.

940 100. Hutchinson, I.B.; Ingle, R.; Edwards, H.G.M.; Harris, L.; McHugh, M.; Malherbe, C.; Parnell, J.
941 Raman spectroscopy on Mars: Identification of geological and bio-geological signatures in
942 Martian analogues using miniaturized Raman spectrometers. *Philos. Trans. R. Soc.* **2014**, *372*,
943 20140204.

944 101. Robinson, J.A.C.; Wood, B.J. The depth of the spinel to garnet transition at the peridotite
945 solidus. *Earth Planet. Sci. Lett.* **1998**, *164*, 277-284.

946 102. Stachel, T.; Harris, J.W. The origin of cratonic diamond-constraints from mineral inclusions. *Ore
947 Geol. Rev.* **2008**, *34*, 5-32.

948 103. Kudoh, Y.; Kurabayashi, T.; Mizobata, H.; Ohtani, E.; Sasaki, S.; Tanaka, M. Pressure
949 dependence of u parameter in ringwoodite up to 7.9 GPa. *J. Miner. Petrol. Sci.* **2007**, *102*, 8-11.

950 104. Ye, Y.; Brown, D.A.; Smyth, J.R.; Panero, W.R.; Jacobsen, S.D.; Chang, Y.Y.; Townsend, J.P.;
951 Thomas, S.M.; Hauri, E.H.; Dera, P.; Frost, D.J. Compressibility and thermal expansion of
952 hydrous ringwoodite with 2.5(3) wt% H₂O. *Am. Mineral.* **2012**, *97*, 573-582.

953 105. Kleppe, A.K.; Jephcoat, A.P.; Smyth, J.R. Raman spectroscopic study of hydrous γ -Mg₂SiO₄ to
954 56.5 GPa. *Phys. Chem. Miner.* **2002**, *29*, 473-476.

955 106. Chopelas, A.; Boehler, R.; Ko, T. Thermodynamics and behavior of γ -Mg₂SiO₄ at high pressure:
956 Implications for Mg₂SiO₄ phase equilibrium. *Phys. Chem. Miner.* **1994**, *21*, 351-359.

957 107. Xie, Z.; Sharp, T.G. High-pressure phases in shock-induced melt veins of the Umbarger L6
958 chondrite: Constraints of shock pressure. *Meteorit. Planet. Sc.* **2004**, *39*, 2043-2054.

959 108. Xie, Z.; Sharp, T.G. Host rock solid-state transformation in a shock-induced melt vein of
960 Tenham L6 chondrite. *Earth Planet. Sci. Lett.* **2007**, *254*, 433-445.

961 109. Nagy, S.; Józsa, S.; Gyollai, I.; Bérczi, S.; Bendő, Z.; Stehlík, H. Ringwoodite microstructures in
962 L-chondrite NWA 5011: Implications for transformation mechanism and source region in L
963 parent body. *Cent. Eur. Geol.* **2011**, *54*, 233-248.

964 110. Sharp, T.G.; Xie, Z.; DeCarli, P.S.; Hu, J. A large shock vein in L chondrite Roosevelt County 106:
965 Evidence for a long-duration shock pulse on the L chondrite parent body. *Meteorit. Planet. Sc.*
966 **2015**, *50*, 1941-1953.

967 111. Tomioka, N.; Okuchi, T. A new high-pressure form of Mg₂SiO₄ highlighting diffusionless phase
968 transition of olivine. *Sci. Rep.* **2017**, *7*, 17351.